

# Extreme Value Analysis of Tidal Stream Velocity Perturbations

Samuel Harding\*, Jim Thomson<sup>†</sup>, Brian Polagye<sup>†</sup>, Marshall Richmond<sup>‡</sup>, Vibhav Durgesh<sup>‡</sup> and Ian Bryden\*

\*School of Engineering, The University of Edinburgh, Scotland, UK

E-mail: s.harding@ed.ac.uk

<sup>†</sup>Northwest National Marine Renewable Energy Center, The University of Washington, Seattle, WA 98105, USA

<sup>‡</sup>Hydrology Group, Pacific Northwest National Laboratory, Richland, WA 99352, USA

**Abstract**—This paper presents a statistical extreme value analysis of maximum velocity perturbations from the mean flow speed in a tidal stream. This study was performed using tidal velocity data measured using both an Acoustic Doppler Velocimeter (ADV) and an Acoustic Doppler Current Profiler (ADCP) at the same location which allows for direct comparison of predictions. The extreme value analysis implements a Peak-Over-Threshold method to explore the effect of perturbation length and time scale on the magnitude of a 50-year perturbation.

**Index Terms**—Tidal Stream, Turbulence, Extreme Value Analysis, Acoustic Doppler Velocimeter

## NOMENCLATURE

$h$	=	Depth of water column
$k_w$	=	Wave number
$k$	=	Number of exceedances
$l$	=	Pareto distribution log-likelihood
$m$	=	Number of observation in $N$ years
$n$	=	Number of observations per year
$p$	=	Declustering threshold
$r$	=	Declustering run length
$t$	=	Time
$u$	=	Velocity perturbation, $U - \langle U \rangle$
$u_t$	=	GPD threshold
$x$	=	Measured values
$y$	=	Threshold excesses, $x - u_t$
$z$	=	Distance from the seabed
$H$	=	Generalized Pareto distribution function
$\tilde{H}$	=	Empirical distribution function
$H_s$	=	Significant wave height
$I$	=	Normalized turbulence intensity
$L$	=	Averaging length scale
$M$	=	Number of observations
$N$	=	Return period
$N_p$	=	Number of pings per ensemble
$T$	=	Temporal averaging period
$T_p$	=	Peak wave period
$U$	=	Principal axis component of velocity
$\zeta_u$	=	Exceedance probability
$\lambda$	=	Wavelength
$\mu$	=	Location factor
$\xi$	=	Shape factor
$\sigma$	=	Scale factor
$\langle \rangle$	=	Mean value

## I. INTRODUCTION

Installations of tidal current energy converters are inherently exposed to highly energetic flow conditions. While the astronomically driven tidal cycles are well understood and can be modeled to predict mean tidal flows, the instantaneous current velocity in the turbulent flow field can be shown to significantly deviate from this [1]. This observation has important implications for numerous design considerations, including the dynamic loading conditions on the turbine blades, support structures and seabed connections. It has also been proposed that hydrodynamic lifting surfaces could be used to stabilize devices on the seabed through the generation of down force from the tidal flow itself [2]. In all of these situations, it is valuable to have an understanding of the magnitude of the maximum velocity perturbations that can be expected in the tidal flow.

## II. DATA ACQUISITION

This analysis was performed using tidal stream flow measurements taken in the Puget Sound, Washington, using ADV and ADCP devices simultaneously. The purpose of the deployment was to compare the performance of ADCP measurements, which are known to have a higher error at sampling rates of the order of 1Hz, against the ADV measurements which are known to be highly accurate at high sampling frequencies. These devices were mounted on a tripod with the ADV sample volume located  $z = 4.8\text{m}$  above the seabed, and the ADCP measuring the adjacent water column in 0.5m bins. In order to compare the measured velocity values, the ADCP bin used in this analysis was centered at 4.71m above the seabed. The operational settings of the two devices is summarized in Table I.

TABLE I  
ACQUISITION SETTINGS OF ADV AND ADCP

	Rate Sample (Hz)	Burst Length (s)	Sampling Interval (min)	Standard Error Velocity (m/s)
ADV	32	64	10	0.04 <sup>1</sup>
ADCP	2	64	30	0.195 <sup>2</sup>

<sup>1</sup> Taken from Nortek Vector deployment software

<sup>2</sup> Taken from RDI's PlanADCP software

A sample of the simultaneous velocity measurements from the two devices is shown in Fig. 1. This plot clearly shows the effect of Doppler noise on the ADCP readings. While the variance can be partially corrected for standard error using Equation 5 from [3], this analysis deals with individual realizations of velocity measurements so this correction cannot be applied. Note that the differences between the ADV and ADCP signals in this figure can be attributed to clock drift on the order of 5s per day.

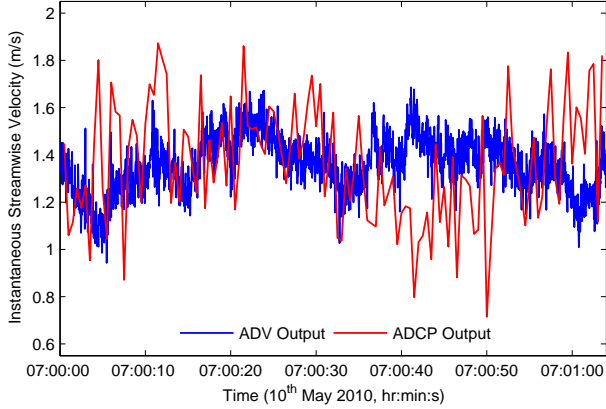


Fig. 1. Comparison of ADV and ADVP velocity time series

The tidal stream velocity at this site reaches 2m/s in peak spring conditions and a mean depth of  $h = 22\text{m}$ . More detailed explanations of the instrumentation tripod deployment can be found in [3] and [4].

### III. DATA PREPARATION

#### A. Orientation of Data

While some tidal stream turbines may be developed with the capacity to vary their orientation, the majority of first generation designs operate in a bidirectional manner aligned with the principal flow direction. As such, the analysis described in this paper was primarily concerned with the flow perturbations along this axis, referred to as the ‘stream-wise’ direction. To begin, the velocity data from both the ADCP and the ADV were rotated from Earth coordinates to the coordinate system aligned with the principal axis ( $U, V, W$ ). The principal axis direction is calculated using a least square regression algorithm, to maximize the flow energy along the axis direction.

As we are interested in the deviation from the mean flow velocity, the flow perturbation in the stream-wise direction is calculated as  $u = U - \langle U \rangle$ . The mean velocity component,  $\langle U \rangle$ , is calculated over the full 64s sample. This allows the use of the maximum amount of points in the averaging calculation for statistical robustness without causing any significant changes in the underlying statistical requirement of stationarity.

Because the perturbation velocities are symmetrically distributed about the mean velocity, only the magnitudes of the perturbations are considered in this paper. The resulting

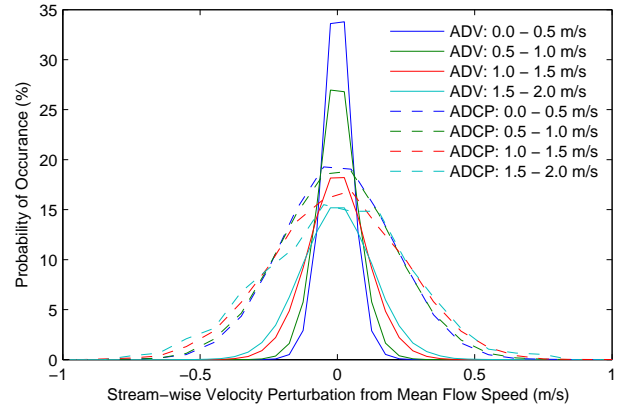


Fig. 2. Distribution of velocity perturbations for different mean flow speeds

extreme perturbation values can then be assumed to occur both above or below the mean velocity.

#### B. Mean Velocity Effects

At flow velocities greater than 1m/s, the normalized turbulence intensity,  $I = \sqrt{\langle u^2 \rangle} / \langle U \rangle$  can be shown to reach a steady state value of approximately 10% in both [3] in Puget Sound (USA) using the present data set, as well as velocity measurements taken in Orkney (UK) [5]. This demonstrates the physical principal whereby larger fluctuations occur at the higher flow speeds. Using all the data in the extreme value analysis in a single data set, the overall maximum fluctuation can be calculated, and it can be implied that this would occur during the maximum flow speed of the site. This is the approach used in the analysis reported in this paper.

It is also of interest to observe how the maximum perturbation changes as a function of the mean flow speed. The distributions of the velocity perturbations divided into 0.5m/s bins of mean velocities are shown in Fig. 2. This plot clearly shows the effect of the significant Doppler noise introduced into the ADCP measurements, discussed further in Section VI-A, by the much wider distribution of fluctuations at all mean flow speeds. The increase in the distribution width as a function of flow speed is also evident. The dependence on flow speed is an interesting subject for future analysis, but is not pursued in this paper owing to the increased error margins attributed to dividing an already limited data set into smaller subsets.

#### C. Time-scale Averaging

Performing an analysis on the raw data collected by the ADV would allow the peak fluctuation with a time-scale of 1/32s to be deduced (0.5s for the ADCP readings). However a fluctuation of such a time-scale is unlikely to have a significant influence on structural loads or hydrodynamic performance. This follows the classical theory of turbulent energy cascade, where Kolmogorov showed that the smaller scales contain the least energy.

To increase the effective duration of the flow perturbation, a central moving average was calculated over the averaging

windows of  $T = \{0.5s, 2.0s, 5.0s, 10.0s\}$ . The velocity perturbation at time,  $t$ , averaged over a temporal window of  $T$  seconds can be expressed mathematically by Equation 1.

$$\langle u(t, T) \rangle = \frac{1}{T} \int_{t-T/2}^{t+T/2} u(t) dt \quad (1)$$

A sample of the instantaneous velocity measurements compared with the 2s averaged values for the ADV is shown in Fig. 3. Because individual points have significant influence on the extreme value analysis, the limits of the data set with insufficient points to average over the full averaging window were discarded (the first and last 32 points in the example shown in Fig. 3).

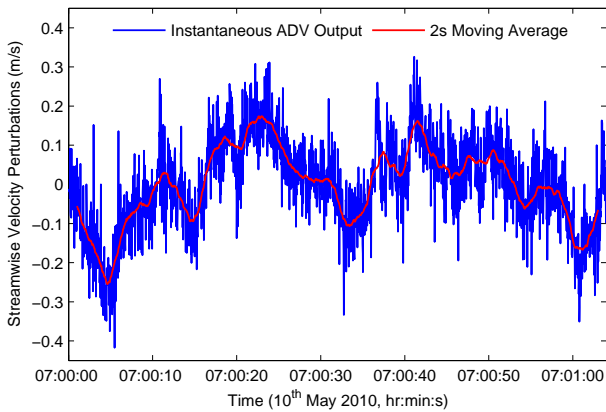


Fig. 3. Comparison of instantaneous and averaged ADV velocities, using temporal averaging window of  $T = 2s$

#### D. Length-scale Averaging

In a similar argument to time-scale averaging, the impact of effective length-scale of the fluctuations is also of interest. Assuming Taylor's hypothesis of frozen turbulence, the temporal window for a moving average with a specified length-scale,  $L$ , must increase as the convection velocity decreases in accordance to the relationship  $T = L / \langle U(t) \rangle$ . The moving average was calculated over the spacial averaging windows of  $L = \{0.5m, 2.0m, 5.0m, 10.0m\}$ .

#### E. Wave Induced Velocity Fluctuations

Waves at the site are fetch-limited from all directions and achieve a maximum state of  $Hs = 1m$ ,  $Tp = 4s$  during a large winter storm. This gives a wavelength of  $\lambda = 25m$  using linear theory, which is be considered as a deep water wave under the condition of  $\lambda/2 < h$ . As such, the orbital velocities decay as a function of  $\cosh(k_w z) / \cosh(k_w h)$  so that the 0.8m/s orbital velocity at the surface will be 0.01m/s at the depth of the ADV. This is an order of magnitude less than the turbulent fluctuations measured by the ADV and so no adjustment for the wave induced velocity fluctuations was made in this analysis.

#### F. Declustering

One of the key assumptions made when using the chosen statistical method for the prediction of extreme values is the independence of data in the set [6]. Generating a data set using the moving average over a specified time or length scale inherently makes each data point dependent on the surrounding values, therefore invalidating this assumption. In order to overcome this, the data was filtered to obtain a set of independent exceedances of a threshold, in a process known as declustering.

The specific declustering technique used is called 'runs declustering' and involves the following procedure. Firstly a threshold,  $p$ , is defined and when a data point exceeds this value, a cluster is started. This cluster is terminated when a specified declustering run length of  $r$  points fall below the threshold. The maximum absolute value of each cluster is recorded, and all other values are set to zero [7].

### IV. EXTREME VALUE ANALYSIS

#### A. An Introduction to the Theory

The Generalized Extreme Value (GEV) Theory describes how the maximum values of independent and identically distributed random variables can be fitted to a singular distribution. This allows their behavior to be extrapolated into the future in the prediction of extreme events. This shape of this distribution is governed by the inputs of a location factor ( $\mu$ ), scale factor ( $\sigma$ ) and shape factor ( $\xi$ ).

The challenge remains to estimate these parameters with very limited duration of data, relative to the 50 year time scale prediction. A key requirement of the GEV theory is that only one value from each observation period (epoch) is used in the model. This is often an inefficient use of data set, which becomes particularly significant when historic data is limited. One modification of the GEV approach is to use a Peak-Over-Threshold (POT) method. This approach is based on the Generalized Pareto Distribution (GPD) and makes use of each data point above a specified threshold [8]. In this way, more information can be extracted from the limited data set, than when only the epoch maximum is used.

Let  $x$  represent a sequence of independent and identically distributed measurements (which in this case are the declustered velocity perturbations), and  $u_t$  represent the threshold selected. The GPD function,  $H$ , describes the distribution function of a variable  $X$  as a function of the threshold excesses ( $y = x - u_t$ ), conditional on  $X > u_t$ , and is described mathematically by Equation 2.

$$H(y) = Pr\{X > x \mid X > u_t\} = \begin{cases} 1 - \left(1 + \frac{\xi y}{\sigma}\right)^{-1/\xi} & \text{when } \xi \neq 0 \\ 1 - \exp\left(-\frac{y}{\sigma}\right) & \text{when } \xi = 0 \end{cases} \quad (2)$$

The values of the shape and scale parameters are calculated by the optimization of the log-likelihood function of

Equation 3 to a maximum, provided  $(1 + \xi y_i/\sigma) > 0$  for  $i = 1, \dots, k$  where  $k$  is the number of threshold exceedances.

$$l(\sigma, \xi) = \begin{cases} -k \cdot \log(\sigma) - (1 + 1/\xi) \sum_{i=1}^k \log(1 + \xi y_i/\sigma) & \text{when } \xi \neq 0 \\ -k \cdot \log(\sigma) - \sigma^{-1} \sum_{i=1}^k y_i & \text{when } \xi = 0 \end{cases} \quad (3)$$

### B. Threshold Selection

One of the main challenges with the GPD method relative to GEV method is the selection of the threshold above which data peaks are considered. The shape and scale factors are highly sensitive to the threshold selection. When the threshold is set very low, the GPD is biased by the values further from the extremes, however setting a very high threshold results in limiting the number of exceedances, leading to excessive variance in the model. One approach recommended in [6] is to plot the optimized shape and scale parameters for a range of possible threshold values, as in Figure 4. Using this technique, the variance of the parameters, and therefore the distribution, can be seen to increase as the threshold increased. The highest threshold which returns stable values of the shape and scale parameters was selected, in a bias-variance trade-off. For the example shown in Figure 4, a threshold of  $u_t = 0.2\text{m/s}$  was selected.

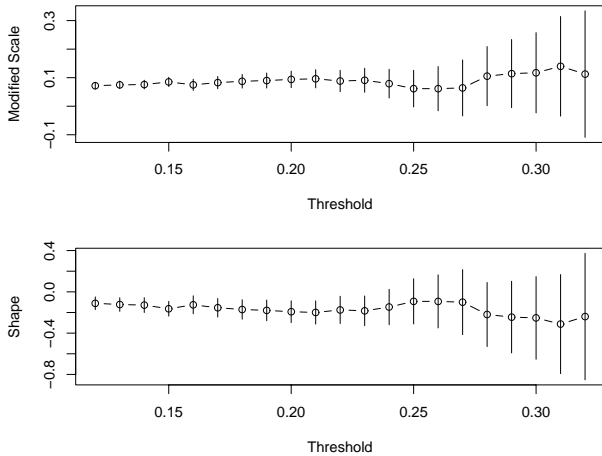


Fig. 4. Stability analysis of GPD parameters with range of thresholds;  $T = 2.0\text{s}$ ,  $p = 0.001\text{m/s}$ ,  $r = 10$

A sample scatter plot of the perturbations over the acquisition time is presented in Figure 5. The selected threshold is shown in blue. For a data set of length  $M$ , the exceedance probability is defined by the parameter  $\zeta_u = k/M$ .

### C. Statistical Analysis Program

The majority of the statistical analyses outlined in this paper were performed using the ‘*extRemes*’ toolkit within

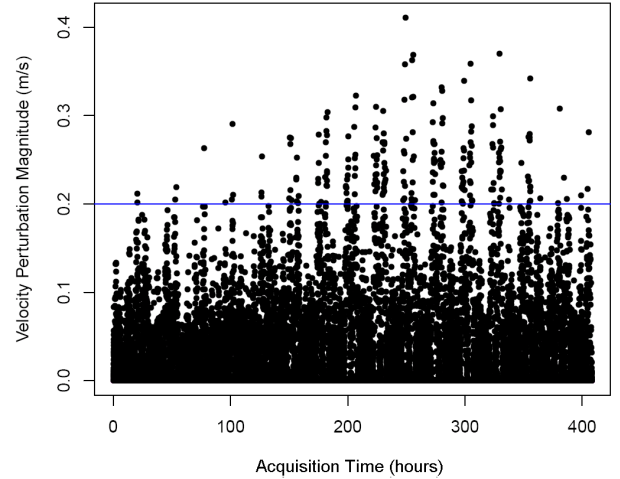


Fig. 5. Example scatter plot indicating threshold selection;  $u_t = 0.20\text{m/s}$ ,  $T = 2.0\text{s}$

the statistical software program *R* [9]. This toolkit is an implementation of many techniques described in [6], and provides a graphical user interface to the ‘*ismev*’ package. More information about the capabilities of the toolbox can be found in [10].

## V. ANALYSIS RESULTS

### A. Analysis Parameters

The extreme value analysis was carried out for the time and length scale variations specified. Runs declustering was performed on the perturbation magnitudes using a declustering threshold of  $p = 0.001\text{m/s}$  and run length of  $r = 10$ . In this way, a new cluster was initiated whenever the perturbation changed direction for longer than 10 data points. For each analysis, the values of  $\sigma$  and  $\xi$  which maximize the log-likelihood expression in Equation 3 are calculated. The results of the analysis is an  $N$ -year return level, defined as the perturbation magnitude that is expected to be exceeded once every  $N$  years. If the number of observations per year is represented by  $n$ , the number of observations in the  $N$  years is  $m = n \times N$  such that an  $N$ -year and an  $m$ -observation return level are interchangeable terms.

### B. Diagnostics Plots

The ‘goodness of fit’ of the resulting GPD model to the real data can be visualized in a number of useful diagnostic plots; the probability plot, quantile plot, density plot, and the return level plot [6]. The inferences made from each plot are briefly described in the following sections and example plots are shown in Figure 6. The coordinates of the information presented in each plot are summarized in Table II.

The probability and quantile plots represent a comparison between the empirical distribution function of  $\hat{H}(x) = i/(k+1)$  for  $x_1 \leq x_i \leq \dots \leq x_k$  and the GPD model. When these two functions are well matched, both of these plots indicate the correlation with a linear scatter plot with

TABLE II  
COORDINATES OF DIAGNOSTIC PLOTS

Probability Plot	$\{(H(x_i), \frac{i}{n+1}) : i = 1, \dots, k\}$
Quantile Plot	$\{(H^{-1}(\frac{i}{n+1}), x_i) : i = 1, \dots, k\}$
Density Plot	$(H, x)$
Return Level	$(N, (u_t + \frac{\sigma}{\xi} ((m\zeta)^\xi - 1)))$

a gradient of unity. The two plots both compare these two functions, but in differing ways, such that one may appear to demonstrate an acceptable fit while the other does not. Firstly, the probability plot provides a direct comparison of the probability of occurrence of a perturbation of a specific magnitude. However, the quantile plot compares the perturbation magnitudes predicted by the two models over the range of probabilities of 0 to 1. In other words, the Probability plot compares the probabilities predicted by the models for the range of perturbation magnitudes, and the Quantile plot compares the perturbation magnitudes predicted by the models for the range of probabilities. In this way, these two plots present the same information on a different scale [6].

The density plot depicts a histogram of occurrences above discrete bands of perturbation magnitudes, normalized by the total number of threshold exceedances. In this way the GPD can be overlaid to observe how closely the model fits the distribution of the threshold excesses.

The return level plot shows the  $N$ -year return level as a function of return period,  $N$ , with associated 95% delta-method confidence intervals. An example is shown in Figure 7. Overlaid on this plot are the magnitudes of the velocity data points plotted against their expected return period. Because the data set being used is 17 days in duration, the greatest return period that can be plotted is  $17/365 = 0.047$  years.

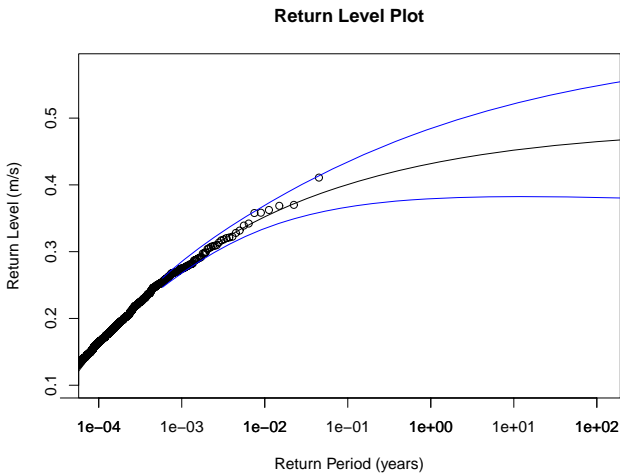


Fig. 7. Sample Return Level plot for ADV perturbations;  $u_t=0.20$ ,  $T=2.0s$

### C. Results Summary

The resulting estimations of 50-year horizontal stream-wise velocity perturbations and associated confidence intervals are shown in Figure 8 and Figure 9. The confidence intervals shown in these plots are based on the variation of the profile log-likelihood with respect to the return level. The delta-method confidence interval shown in the return level plot is a symmetrical and un-conservative method of calculating the variance. The profile log-likelihood confidence interval, on the other hand, incorporates the skew in variance which has the effect of excluding the possibility of including a perturbation magnitude less than the maximum observed fluctuation. In this way the profile log-likelihood confidence interval offers a more realistic approximation of the expected errors [6].

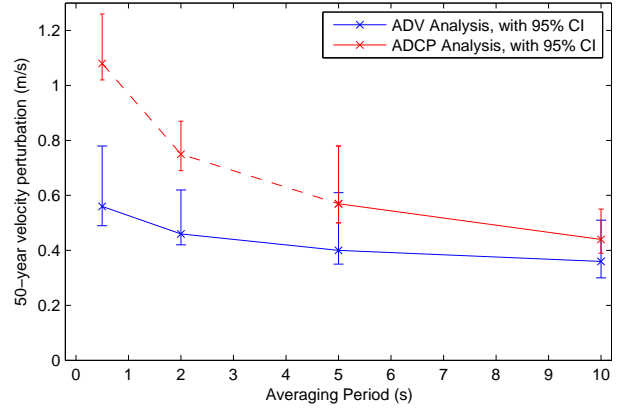


Fig. 8. Effects of perturbation time-scale on the 50-year velocity perturbation magnitude

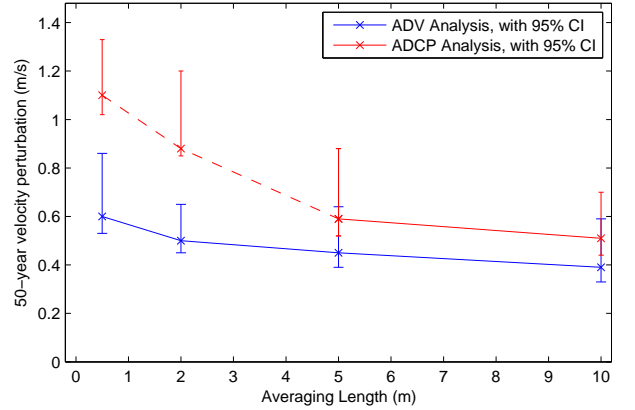


Fig. 9. Effects of perturbation length-scale on the 50-year velocity perturbation magnitude

## VI. DISCUSSION AND LIMITATIONS

### A. Discrepancies between ADV and ADCP results

The results of the extreme value analysis show obvious discrepancies between the two data sets. This is primarily due to the more significant Doppler noise in the ADCP

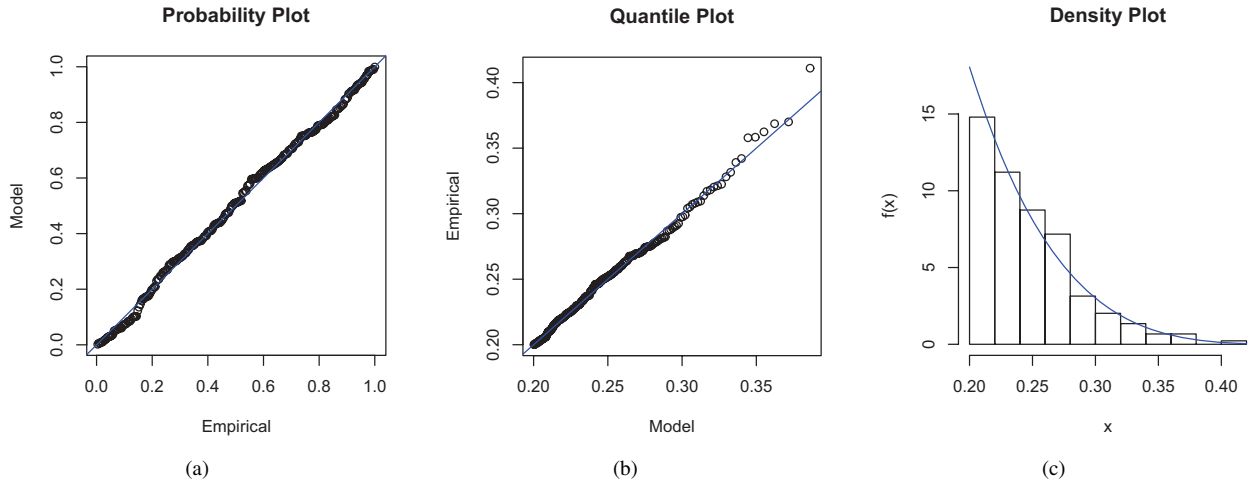


Fig. 6. Diagnostic Plots for GPD calculated for ADV velocity perturbations;  $u_t=0.20$ ,  $T=2.0s$ ,  $p=0.001m/s$ ,  $r=10$

measurement (Table I). The maximum sampling frequency of the ADCP at 2Hz also contributes to the greater variance as fewer points are averaged for both the time and length scale analyses. With significantly less Doppler noise and greater sampling rates, the results of the analysis using the ADV data are taken as the benchmark of accuracy, and any discrepancy is attributed to these limitations of ADCP operation. Again, when the standard deviation of the velocity is of interest, in the calculation of turbulence intensity, the distribution can be partially corrected for the standard error of the device as explained in [3]. However, this could not be implemented in this analysis where the individual instances of the velocity measurements were of interest.

Figure 8 and Figure 9 show that the ADCP analysis significantly over-estimates the extreme value predictions beyond the confidence interval of the ADV analysis for averaging scales less than 5s and 5m (indicated with a red dashed line). From this we can infer that in this range, the ADCP results are invalid, with no statistical similarity to the ADV benchmark.

Doppler noise theoretically decreases with  $1/\sqrt{N_p}$ , with  $N_p$  being the number of pings in the ensemble, and this is responsible for the convergence of results over longer time and length scales. However the difference between the standard error of the ADCP and ADV is significant over all ensemble durations used in this analysis, as shown in Figure 10. While the averaging period of 5s results in a noise reduction to 32% of the raw ADCP measurement error (when  $N = 10$ ), this is still almost twice that of the ADV without any averaging. The influence of Doppler noise on the distribution of simulated turbulence intensities is examined in greater detail in [11]. As the averaging window tends to 64s, the extreme fluctuations approach zero as expected.

Interestingly, the differing beam configurations of the two devices act to decrease the velocity fluctuations of the ADCP relative to the ADV. The beams of an ADV are convergent to enable the velocity coordinates of a very small volume to be deduced. Conversely, the ADCP beams are directed in

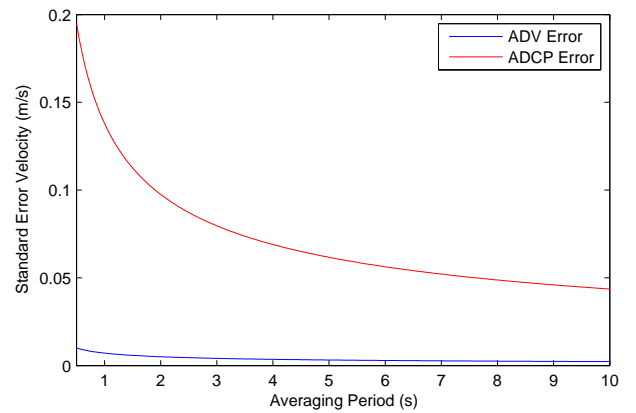


Fig. 10. The influence of averaging period on Doppler uncertainty

a diverging configuration. The underlying assumption of the ADCP is that the flow is homogeneous over the sample area, such that a velocity component measured by each beam in each different location can be transformed to calculate the velocity components of one location, notionally centralized above the ADCP device [12]. As such, the velocity component measured in each beam bin are effectively averaged through the vector transformation process. This has the effect of decreasing the measured velocity perturbations. In other words, without accounting for Doppler uncertainty, one would expect the ADV data to show stronger perturbations.

### B. Shape Factor

The key similarity between all observations was the shape factor consistently being optimized to a value below zero. In accordance with Equation 2, the return level increases exponentially with the return period when  $\xi > 0$ , linearly when  $\xi = 0$ , and reaches an asymptotic limit when  $\xi < 0$  of  $u_t - \sigma/\xi$ . In all extreme value analyses performed,  $\xi < 0$ , resulting in the asymptotic behavior shown in Figure 7.

### C. Duration of Data Set

The key limitation to this analysis is the length of data acquisition from both of the devices. It is very difficult to predict a 50-year event from one month of data, and this has resulted in significant confidence intervals in the expected values. Ideally, several years of data is required to perform the analysis to an acceptable level of confidence. With the recent increase of interest in instrumentation of tidally energetic sites for the application of tidal stream power, this may be a possibility in the future. However the present analysis offers a useful starting point for ongoing analysis.

## VII. CONCLUSION

This paper presents an extreme value analysis using velocity perturbations measured using both ADV and ADCP devices mounted on a large instrumentation tripod in an energetic tidal stream. The results indicate large discrepancies between the measurements of the two devices, owing primarily to the increased Doppler noise of the ADCP readings. This observation is important to recognize in a time when ADCPs are increasingly being used to measure flows in tidal energetic flows in the context of tidal stream power. While proven to effectively measure the mean flow velocity over long averaging periods, this data analysis highlights the risk of over-conservative design decisions if these instruments are used to define extreme events.

A 50-year velocity perturbation from a 64s mean velocity was predicted to range between 0.30m/s and 0.78m/s over the range of temporal averaging periods examined in the analysis, to 95% confidence. The ADCP perturbations consistently exceeded that of the ADV predictions, though convergence of results is apparent at higher averaging durations. Significant confidence intervals are included in the presentation of the results which will be reduced with continued measurement of high frequency point measurements.

## ACKNOWLEDGMENT

The Puget Sound field measurements were funded by the US Department of Energy, Energy Efficiency and Renewable Energy, Wind and Water Power Program. Samuel Harding wishes to acknowledge the Tertiary Education Commission of New Zealand for the funding of his research at the University of Edinburgh and Ewan Dawson of the British Geological Survey for his contribution to the statistical analysis.

## REFERENCES

- [1] B. Polagye, J. Epler, and J. Thomson, "Limits to the predictability of tidal current energy," in *OCEANS 2010*, 2010, pp. 1–9.
- [2] A. Owen and I. Bryden, "Prototype support structure for seabed mounted tidal current turbines," *Proceedings of the Institution of Mechanical Engineers Part M: Journal of Engineering for the Maritime Environment*, vol. 219, no. 4, pp. 173–183, 2005.
- [3] J. Thomson, B. Polagye, M. Richmond, and V. Durgesh, "Quantifying turbulence for tidal power applications," in *OCEANS 2010*, Seattle, WA, 2010.
- [4] M. Richmond, J. Thomson, V. Durgesh, and B. Polagye, "Inflow Characterization for Marine and Hydrokinetic Energy Devices: FY-2010 Annual Progress Report," Pacific Northwest National Laboratory, Richland, WA, Tech. Rep. PNNL-19859, 2011.
- [5] G. McCann, M. Thomson, and S. Hitchcock, "Implications of site-specific conditions on the prediction of loading and power performance of a tidal stream device," in *2nd International Conference on Ocean Energy*, Brest, France, October 2008.
- [6] S. Coles, *An Introduction to Statistical Modeling of Extreme Values*, 1st ed. Springer, 2001.
- [7] E. Gilleland, R. Katz, and G. Young. (2010, April) Extreme value toolkit: Package 'extremes'. [Online]. Available: <http://cran.r-project.org/web/packages/extRemes/extRemes.pdf>
- [8] J. Palutikof, B. Brabson, D. Lister, and S. Adcock, "A review of methods to calculate extreme wind speeds," *Meteorological Applications*, vol. 6, no. 2, pp. 119–132, 1999.
- [9] R Development Core Team, "R: A Language and Environment for Statistical Computing," Vienna, Austria, 2009. [Online]. Available: <http://www.r-project.org>
- [10] The National Center for Atmospheric Research. (2007) Extremes toolkit. [Online]. Available: <http://www.assessment.ucar.edu/toolkit/>
- [11] B. Polagye and J. Thomson, "Calculation of turbulence intensity from doppler current measurements," in preparation.
- [12] *Acoustic Doppler Current Profiler: Principles of Operation - A Practical Primer*, 2nd ed., RD Instruments, California, USA, 1996.